# Nonvolatile electric field control of spin-valley-layer polarized anomalous Hall effect in a two-dimensional multiferroic semiconductor bilayer

Li Feng, Xiaofang Chen,[*] and Jingshan Qi [†]

*School of Physics and Electronic Engineering, Jiangsu Normal University, Xuzhou 221116, People's Republic of China*

The coupling of the lattice, charge, spin, and valley degrees of freedom is a fundamental scientific issue in spintronics and valleytronics. The nonvolatile electric field control of the spin and valley polarization has important potential applications for the development of next-generation ultrahigh speed processors and memories. However, the efficient electrical control of spin and valley degrees of freedom remains a challenge due to the weak coupling between them and external electric fields. Here we report the strong coupling between the spin, valley, and electric polarization in a two- dimensional multiferroic material $Nb_3I_8$ with a breathing Kagome lattice. The ferroelectric transition controls the local sublattice symmetry in the ferroelectric monolayer $Nb_3I_8$ and thus results in the sublattice-dependent Berry curvature switching in the momentum space, where the sign reversal of the Berry curvature can be controlled by reversing the ferroelectric polarization. More importantly, for the ferroelectric bilayer $Nb_3I_8$ with A-type antiferromagnetic coupling, the spin-valley-layer polarized anomalous Hall effect can be realized by coupling the electric polarization to spin, valley and layer degrees of freedom. So, the electrically driven the ferroelectric transition in a $Nb_3I_8$ bilayer can be applied to design nonvolatile memory and switch based on the spin, valley and layer dependent Berry curvature. Our findings open an avenue towards exploring the coupling between the ferroelectricity, ferromagnetism, and ferrovalley in the hidden local sublattice symmetry and demonstrate a nonvolatile electric-field controlled anomalous Hall effect in the atomically thin limit.

## I. INTRODUCTION

Two-dimensional (2D) layered materials often exhibit exotic quantum phases due to the delicate coupling and competitions of various degrees of freedom such as the charge, lattice, orbital, and spin [1–4]. Valley, as an electronic degree of freedom, has received considerable attention in recent years due to its important implications in both basic quantum physics and advanced information technology [5–10]. Atomically thin monolayer transition metal dichalcogenides possess the coupling of spin and valley degrees of freedom due to the strong spin-orbit interaction and broken inversion symmetry which gives rise to a series of exotic valley effects [6,11,12]. Usually, external means are needed for controlling the valley degrees of freedom, including the circularly polarized optical excitation [13–15], external magnetic field [16–20], external electric field [21], optical Stark effect [22], magnetic doping [23–29], and magnetic proximity effect [30–34]. All the above methods have a fatal limitation, that is, volatility. When the external field is removed the system immediately returns to the initial paravalley state. Very recently, Liu *et al* [9]. found that the ferromagnetism and sliding ferroelectricity in the bilayer $VS_2$ can be coupled together via the ferrovalley, so as to realize the electric control of magnetism. These studies are of great significance for understanding and manipulating

the interaction between the charge, spin and valley degrees of freedom.

2D multiferroic materials with the coexistence and coupling of multi ferroic orders have attracted a great deal of attention due to the basic physics and potential applications [35–39]. A series of multiferroic materials have been predicted theoretically [40–43] and some have been verified experimentally [43,44]. If the material has the coupled ferroelectricity, ferromagnetism and ferrovalley, the nonvolatile electric field control of the spin and valley degrees of freedom can be realized. This is of great significance for designing the nonvolatile memory and switching devices using the spin and valley degrees of freedom. In this work, we propose a strategy to realize the coupling between the spin, valley and layer degrees of freedom and the nonvolatile electric field control of the spin-valley-layer polarized anomalous Hall effect in a 2D multiferroic $Nb_3I_8$ bilayer with the breathing Kagome lattice. The ferroelectric (FE) polarization controls the local sublattice symmetry in the monolayer $Nb_3I_8$. This results in a sublattice-dependent Berry curvature change in momentum space, where the sign reversal of the Berry curvature can be controlled by the FE polarization. More importantly, for the bilayer $Nb_3I_8$ with A-type antiferromagnetic (AFM) coupling, the spin-valley-layer polarized anomalous Hall effect can be realized by the pure electric filed. So, the layer, spin and valley dependent Berry curvature in the bilayer $Nb_3I_8$ can be applied to design nonvolatile memory and switch. These findings demonstrate a different nonvolatile electric-field controlled anomalous Hall effect in 2D layered materials, which

---

*chenxf@jsnu.edu.cn
†qijingshan@jsnu.edu.cn

has important application potential in the field of information storage.

## II. COMPUTATIONAL METHODS

All calculations are performed based on density functional theory (DFT) [45] implemented in the Vienna *Ab initio* Simulation Package (VASP) [46]. The projector-augmented wave pseudopotentials method [47] and the generalized gradient approximation (GGA) in the Perdew-Burke-Ernzerhof form [48] have been applied. The plane-wave cutoff energy was set to be 350 eV. The structures are relaxed until the force on each atom is less than 0.01 eV/Å. The electronic iteration convergence criterion is set to $1 \times 110^{-6}$ eV. For the geometry optimization, the DFT-D2 method of Grimme [49,50] was considered for taking the van der Waals interaction into account. The Brillouin zone was sampled using an $8 \times 8 \times 1$ Monkhorst-Pack $k$-point grid [51] for the FM states, and a $4 \times 4 \times 1$ grid for the $2 \times 2$ supercell used for the AFM states. An adequate vacuum space of $\sim 20$ Å was set between periodic replicas along the direction orthogonal to the planes (assumed to be the z direction), in order to avoid spurious interactions induced by the periodic boundary conditions. It is well known that GGA function cannot adequately describe the strong correlated systems which contained the partially filled $d$ subshells. To describe the on-site Coulomb repulsion of Nb $4d$ electrons, the GGA $+ U_{\mathrm{eff}}$ method has been considered [52–54]. Based on previous reports for a $Nb_3I_8$ monolayer [55], we set $U_{\mathrm{eff}}$ as 2 eV. We also verified the different $U_{\mathrm{eff}}$ values (from 1 to 3 eV) and confirmed that our conclusion and proposed physical mechanism remain qualitatively unchanged [56]. The spin orbit coupling (SOC) is incorporated in electronic structure calculations. The FE switching pathway was obtained by using the climbing image nudged elastic band (CINEB) method [57,58]. The Kohn-Sham Bloch wave functions on the discretized $k$ mesh are extracted to calculate the Berry curvature [59].

## III. RESULTS AND DISCUSSIONS

### A. Structural symmetry and ferroelectricity

$Nb_3I_8$ crystallizes in the trigonal crystal system with the rhombohedral space group $R\bar{3}m$ and has 2D crystalline structure with very weak interlayer van der Waal interaction [60–62], as shown in Fig. 1(a). Similar to graphene and transition metal dichalcogenides, they can be thinned down to 2D monolayer limit via mechanical exfoliation [55,62,63]. Importantly, the Nb atoms in each monolayer form a breathing Kagome lattice and are sandwiched between the top and the bottom I-atom layer. Also, every three Nb atoms assembles into a $Nb_3$ trimer in monolayer, leading to two kinds of different Nb-Nb distances and triangles as shown in Fig. 1(b). The Nb-Nb distance in the trimer is 3.02 Å, and the Nb-Nb distance between the trimers is 4.66 Å, resulting in the distorted octahedral environment of I atoms. In this way, the structure forms a breathing Kagome Nb-atom network composed of bigger equilateral triangles and smaller equilateral triangles [64]. In a ideal octahedral crystal field, $d$ orbital of Nb atom splits into the double degenerate $e_g$ and triple degenerate $t_{2g}$ orbitals. When the $Nb_3$ trimer are formed, due

to the distorted octahedral environment of I atoms, the orbital degeneracy will be further lifted. Each $Nb_3$ trimer contributes seven electrons and thus generates a magnetic moment of $1\mu B$ due to an unpaired electron. Therefore, the $Nb_3$ trimer can be seen as a superatom with $1\mu B$ magnetic moment per trimer [55,63]. Although the magnetic properties of $Nb_3I_8$ have not been measured experimentally, several theoretical analyses and first-principless calculations have predicted that the monolayer is a ferromagnetic semiconductor [55,63,65]. Our calculations also indicate that the magnetic ground state of the monolayer is ferromagnetic and the magnetic anisotropic energy is small with a energy difference of 0.25 meV/Nb between the out-of-plane and in-plane direction, which are consistent with previous studies [66]. The small magnetic anisotropy indicates that the magnetization direction can be easily controlled by applying a magnetic field.

However, more importantly we find that the trimerization of Nb atoms results in different horizontal heights of I atoms in the out-of-plane direction as shown in Fig. 1(b) and thus break the mirror symmetry. So, the monolayer $Nb_3I_8$ is a FE semiconductor with the out-of-plane vertical polarization and the point group of $C_{3v}^1$. By controlling the trimerization distribution of Nb atoms, the polarization direction can be reversed due to the asymmetric movement of I atoms. The electric polarization of $Nb_3I_8$ monolayer is $0.489 \times 10^{-12}$ C/m, which is comparable to the polarization values of $Ti_3Cl_8$ ($0.641 \times 10^{-12}$ C/m), $Ti_3Br_8$ ($0.644 \times 10^{-12}$ C/m) and $Ti_3I_8$ ($0.579 \times 10^{-12}$ C/m) [64]. 2D FE semiconductors with the out-of-plane FE polarization are the preferred materials for building low energy consumption, high integration, and nonvolatile switching and memory devices. These types of FE materials with the out-of-plane polarization are very rare, and only a few such as $CuInP_2S_6$ [67,68] and $\alpha - In_2Se_3$ [69] have been verified in experiments. Following the approach in Refs. [70–72], we use the classical Monte Carlo (MC) method to estimate FE transition temperature. Our calculated transition temperature is 3500 K [56]. In the following, we firstly propose a mechanism through a general theoretical model to show the effect of the local structural symmetry on the Berry curvature in a 2D system, e.g., $Nb_3I_8$ monolayer.

### B. Theoretical model and Berry curvature of monolayer $Nb_3I_8$

Berry curvature is a fundamental concept in condensed matter physics, which is related to various exotic topological phenomena such as the anomalous Hall effect and valley Hall effect. Generally, to obtain the nonzero Berry curvature in a system, either the time-reversal symmetry or inversion symmetry needs to be broken. A simple model to show this physical mechanism is a 2D honeycomb lattice with two sublattices A and B, as shown in Figs. 1(c) and 1(d). It has a pair of degenerate valleys in the band structure near the $K_+$ and $K_-$ points at opposite corners of the hexagonal Brillouin zone in Figs. 1(g) and 1(h), which gives rise to the valley-contrasting physics and potential applications associated with the nonzero Berry curvature in Fig. 1(e) and 1(f). A low-energy Hamiltonian (LEH) [5,11] can be used to describe electric structure near the valleys, $H = v_F(\tau_z \sigma_x k_x + \sigma_y k_y) + \frac{\Delta}{2}\sigma_z$. Here $k$ is the electronic momentum and $v_F$ the Fermi velocity. $\vec{\sigma}$ and $\vec{\tau}$ are Pauli matrices with $\sigma_z = \pm 1$ describing states on the A(B)
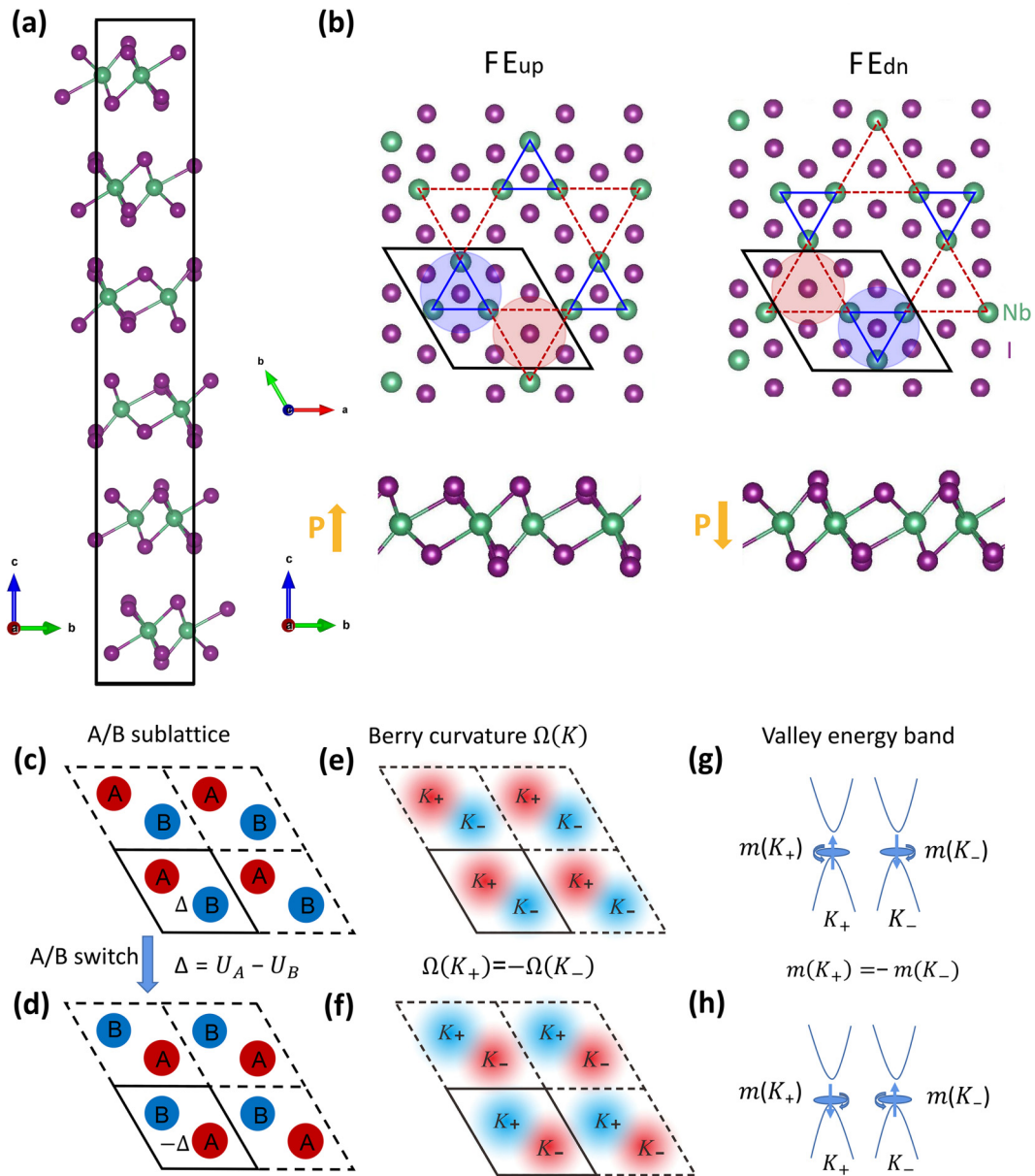
FIG. 1. Schematic diagram of the structure of $Nb_3I_8$. (a) Side view of the bulk $Nb_3I_8$ crystal structure. (b) Top and side views of the breathing Kagome network of monolayers with opposite polarization directions. Nb atoms are in green, and I atoms are in purple. The direction of polarization is uniformly marked with yellow arrows. The Nb trimers are indicated by blue solid line triangles. (c), (d) 2D honeycomb lattice with two sublattices A and B. (e), (f) Berry curvature distribution in momentum space. $K_+$ and $K_-$ points are at opposite corners of the hexagonal Brillouin zone. (g), (h) Valley band and valley magnetic moment m(k) near the $K_+$ and $K_-$ points.

sublattice and $\tau_z = \pm 1$ describing states at the $K_+(K_-)$. The $\frac{\Delta}{2}\sigma_z$ term corresponds to a staggered sublattice potential with a site energy difference $\Delta$ between sublattices which breaks the inversion symmetry and thus opens a gap of $\Delta$. This term is odd under parity, and thus changes sign when the A and B sublattices are interchanged, as shown in Fig. 1(d), leading to the change of Berry curvature distribution in the momentum space in Fig. 1(f).

From the LEH model the momentum-dependent berry curvature can be expressed as $\Omega(k) = \tau_z \frac{2\Delta v_F^2}{(\Delta^2 + 4k^2 v_F^2)^{3/2}}$. Another valley contrasting quantity is the valley magnetic

moment $m(k) = \tau_z \frac{e\Delta v_F^2}{\hbar(\Delta^2 + 4k^2 v_F^2)}$, which reaches its maximum value $m(K_\pm)$ at the point $K_\pm$. When $\Delta$ changes sign from positive to negative, $\Omega(k)$ and $m(k)$ will also change sign for a certain valley, as shown in Figs. 1(f) and 1(h). This provides a method to control berry curvature distribution in the momentum space which will result in some important topological-related physical properties. However, for a certain material with a fixed A/B sublattice, $\Delta$ is usually a constant value (e.g., $h$-BN monolayer) and thus it is difficult to tune by simple electrical/magnetic methods. A feasible scheme is to design a two-dimensional FE material in which the positions
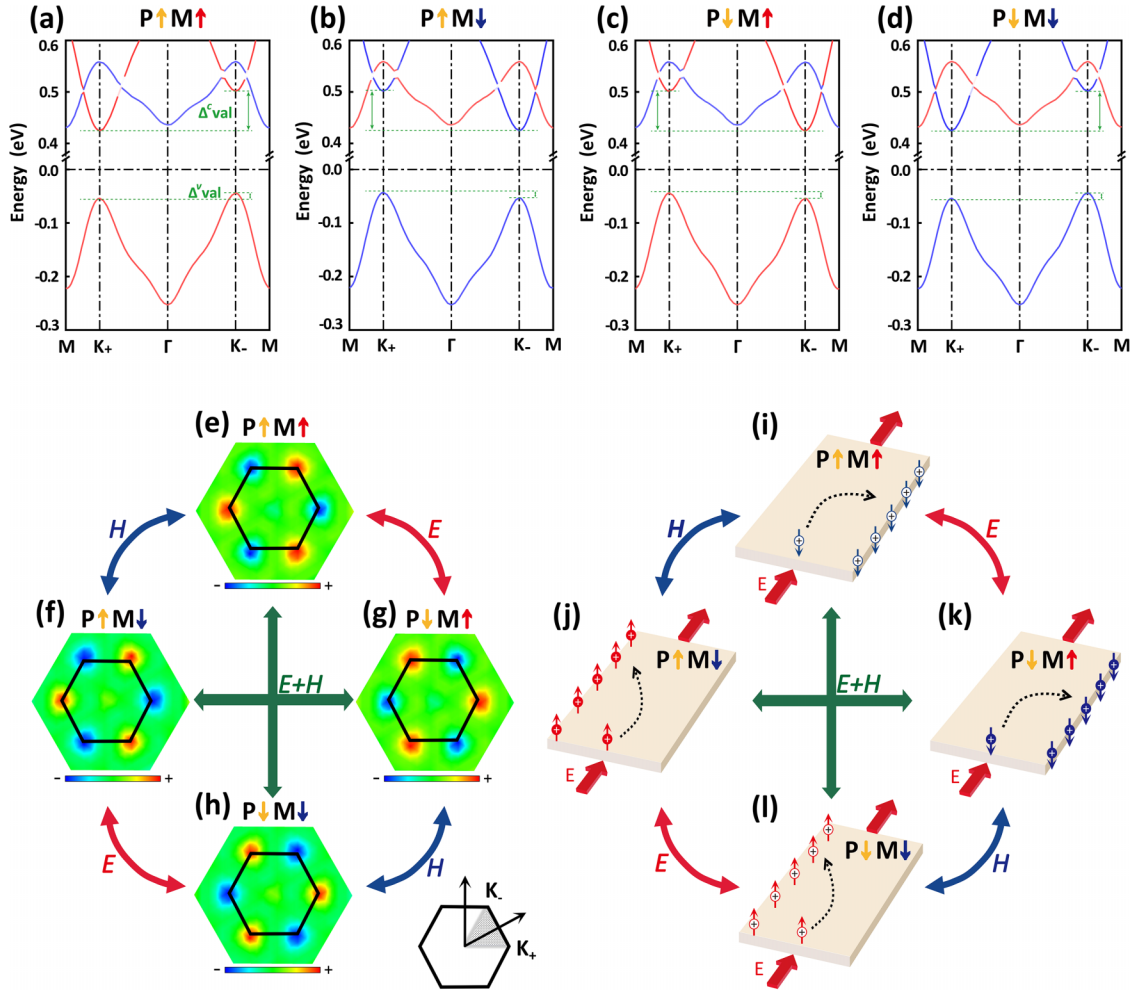
FIG. 2. Energy bands of the $Nb_3I_8$ monolayer with the SOC. Depending on the direction of the polarization and magnetization, four configurations can be distinguished: (a) $P \uparrow M \uparrow$, (b) $P \uparrow M \downarrow$, (c) $P \downarrow M \uparrow$, (d)$P \downarrow M \downarrow$. The red (blue) colors represent the bands of the spin projection in the positive (negative) directions of the z axis. (e)–(h) Berry curvatures calculated for (e) $P \uparrow M \uparrow$, (f) $P \uparrow M \downarrow$, (g) $P \downarrow M \uparrow$, (h) $P \downarrow M \downarrow$ configurations. (i)–(l) Schematic diagrams of anomalous Hall effects for (i) $P \uparrow M \uparrow$, (j) $P \uparrow M \downarrow$, (k) $P \downarrow M \uparrow$, (l) $P \downarrow M \downarrow$ configurations. The solid circles (hollow circles) indicate the holes in the $K_+ (K_-)$ valley, and the upward red (downward blue) arrows represent the holes with spin-up (spin-down) states. The red (blue) curved arrows indicate the change of Berry curvature and hole transport processes under an applied external electric field $E$ (magnetic field $H$), while the green straight arrows denote the change under simultaneous action of $E$ and $H$.

of the two sublattices can be interchanged by the inversion of FE polarization. In this work, we find that the sign of $\Delta$ can be indeed changed by FE switching in a FE monolayer $Nb_3I_8$ with the breathing Kagome lattice and out-of-plane polarization. In a simplified way, $Nb_3I_8$ monolayer can be modeled as a 2D honeycomb lattice with two sublattices, as shown in Fig. 1(b). In a unit cell, one sublattice is composed of a $Nb_3$ trimer and four nearby I atoms as labeled by the blue circular shaded area and the other is formed by four I atoms as labeled by the red circular shaded area. Under such a condition, the inversion symmetry is broken due to two different sublattices. Two opposite polarization directions corresponds to the interchange of two nonequivalent sublattices. Therefore, the sublattice-interchange transition can be realized by FE switching in $Nb_3I_8$ monolayer, leading to the sign reversal of $\Delta$ and Berry curvature. In addition, based on the symmetry argument, the two opposite FE states are

related to each other through an inversion operation. Under the time-reversal, $\Omega(k) = -\Omega(-k)$, and under the FE reversal, $\Omega(k) = \Omega(-k)$ because the $P \uparrow$ and $P \downarrow$ configurations are inversion partners. Thus, $\Omega(k)$ must reverse its sign when the polarization is reversed [73–75]. The band structures near the Fermi level and Berry curvature from the first-principless calculations are shown in Figs. 2(a)–2(h). By comparison, we find that these results are clearly qualitatively consistent with those from the LEH model on 2D honeycomb lattice with two sublattices, as shown in Figs. 1(c)–1(h), indicating that this simplified model describes well the low-energy electric structure of $Nb_3I_8$ monolayer.

The monolayer $Nb_3I_8$ can be divided into four types, $P \uparrow M \uparrow$, $P \uparrow M \downarrow$, $P \downarrow M \uparrow$, and $P \downarrow M \downarrow$, according to the different polarization and spin directions, where $P \uparrow$ $(P \downarrow)$ indicates the FE polarization direction and $M \uparrow (M \downarrow)$ denotes the direction of magnetic moment. Through the
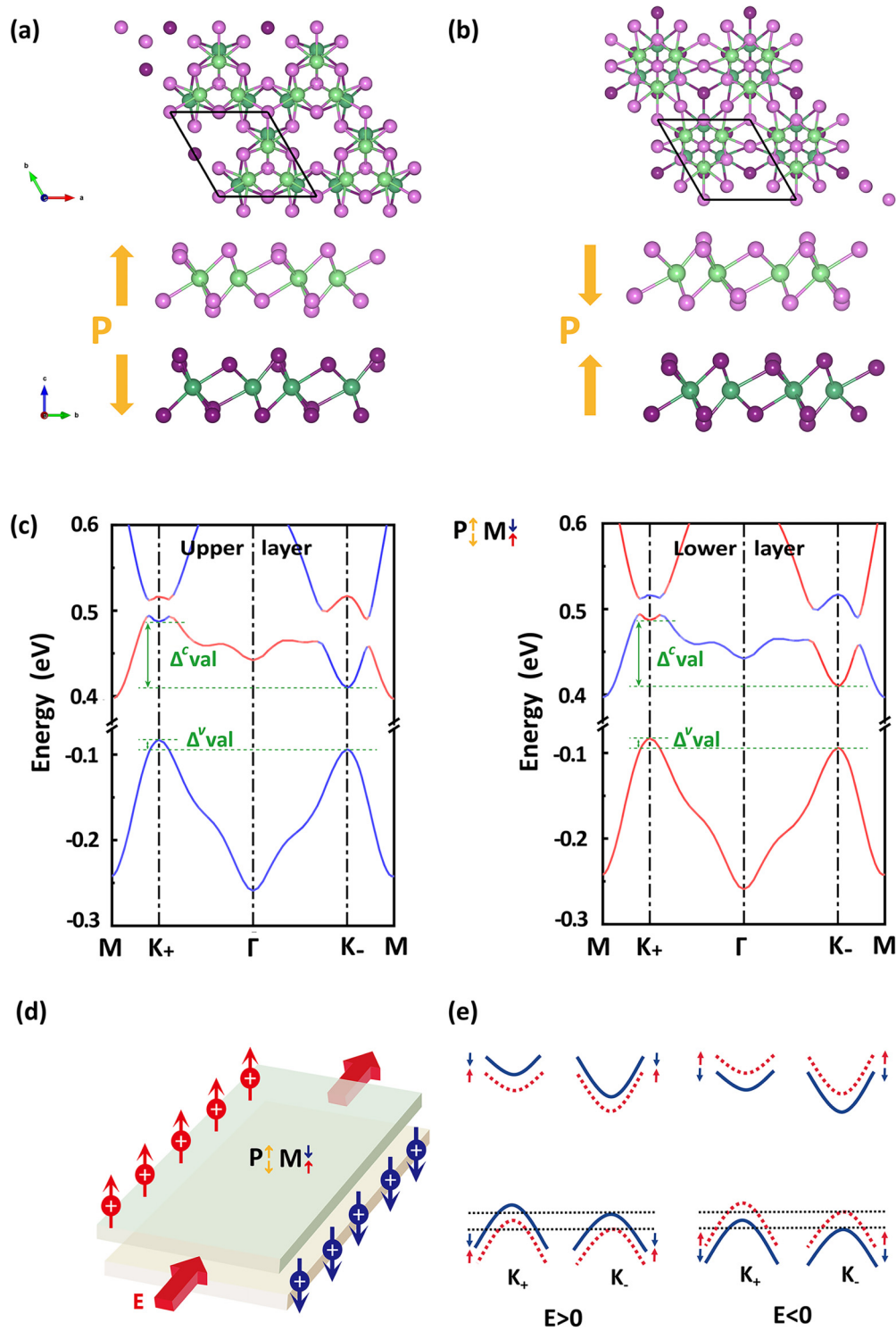
FIG. 3. Side and top views of the bilayer $AFE_{tt}$ (a) and $AFE_{hh}$ (b). The light green and light purple balls represent, respectively, the Nb and I atoms in the upper layer, while the dark green and dark purple balls denote, respectively, the Nb and I atoms in the lower layer. (c) Layer-resolved band structures of the $P\uparrow\downarrow M\uparrow\downarrow$ configuration with the SOC. The left side indicates the energy band contributions of the upper layer and the right side indicates the energy band contributions of the lower layer. (d) Under hole doping the layer-resolved spin Hall effect of the $P\uparrow\downarrow M\uparrow\downarrow$ configuration. (e) The schematic band structures under a positive or negative perpendicular electric field. The red and blue curves represent respectively the spin-up and spin-down bands.

first-principles calculations, we found that these four configurations are degenerate in energy. As shown in Figs. 2(a)–2(d), the energy valley degeneracy at $K_+$ and $K_-$ points is removed when the SOC is considered [56], resulting in a long-sought spontaneous valley splitting, ferrovalley [6]. When the magnetism direction is reversed the valley splitting is opposite, which is consistent with previous results [66]. To characterize the spontaneous valley splitting, we define $\Delta_{val}^v = E_{K_-}^v - E_{K_+}^v (\Delta_{val}^c = E_{K_-}^c - E_{K_+}^c)$ as the energy difference between the $K_-$ and $K_+$ valleys for the highest valence band (lowest conduction band). $\Delta_{val}^v$ and $\Delta_{val}^c$ are, respectively, 10 and 78 meV, which are comparable with those of $VAgP_2Se_6$ (15 meV) [76], $LaBr_2$ (33 meV) [77], $MnPX_3$ (43 meV) [78]. Another important discovery is when the polarization direction is reversed (the magnetism direction is unchanged), the valley splitting is also opposite.

Furthermore, we calculated the Berry curvature in the momentum space, as shown in Figs. 2(e)–2(h). As a pseudo-magnetic field in the momentum space, Berry curvature has a great influence on the electronic transport properties and is the core parameter of various intrinsic Hall effects [79]. When an in-plane longitudinal electric field is applied, the group velocity of electrons will obtain an additional transverse velocity, $v_a \sim E \times \Omega(k)$, where $E$ is the applied in-plane longitudinal electric field and $\Omega(k)$ is the Berry curvature of the Bloch electron. The signs of Berry curvatures at $K_+$ and $K_-$ points are opposite and thus the carriers in the $K_+$ and $K_-$ valleys gain anomalous velocities in the opposite direction. By electron doping or hole doping, the carriers from a certain energy valley will be dominant due to the spontaneous valley splitting, resulting in the anomalous valley Hall effect, as shown in Figs. 2(i)–2(l). For example, in the case of $P \uparrow M \uparrow$, under the hole doping the spin-down holes from the $K_-$ valley acquire a transverse anomalous velocity and generate a spin- and valley-polarized anomalous Hall effect. When only the magnetism direction is reversed, the spin-up holes from the $K_+$ valley acquire a opposite transverse velocity, resulting in the opposite spin- and valley-polarized anomalous Hall effect in the case of $P \uparrow M \downarrow$. When only the polarization direction is reversed in the case of $P \downarrow M \uparrow$, the spin-down holes from the $K_+$ valley acquire a unchanged transverse velocity due to the simultaneously sign change of the valley splitting and Berry curvature. Although in the monolayer the sign of the anomalous Hall voltage is unchanged under the reversal of electric polarization, the FE polarization will has a significant effect on the spin and valley polarized anomalous Hall effect for the bilayer system, as revealed in the following.

### C. Layer-resolved spin Hall effect in AFE bilayer $Nb_3I_8$

Based on the above analysis, we consider the $Nb_3I_8$ bilayer by directly taking out two layers from the bulk. In bulk, the polarization coupling between adjacent layers is antiferroelectric (AFE), as shown in Fig. 1(a). We find that there two different AFE configurations. One is called as the head-to-head AFE configuration($AFE_{hh}$), and the other is defined as the tail-to-tail AFE configuration($AFE_{tt}$), as shown in Figs. 3(a) and 3(b). By the first-principles total energy calculations, we found that the total energy of the $AFE_{tt}$ is lower by 24.7 meV/unit cell than that of the $AFE_{hh}$. In

addition, we also consider other AFE configurations by the interlayer sliding and found that the $AFE_{tt}$ from bulk is the most stable configuration, as shown in Fig. 3(a). For the $AFE_{tt}$ bilayer, we determine the most stable magnetic ground state by considering different magnetic configurations [56]. The results indicate that the magnetic ground state is the intralayer FM and interlayer AFM configuration (A-type AFM), similar to $CrI_3$ [80,81]. The interlayer magnetic exchange energy (defined as $E_{ex} = E_{FM} - E_{AFM}$) is 3 meV/unit cell, comparable with 4 meV($-10$ meV) of AB'(AB) stacked $CrI_3$ [80,82]. Based on the Heisenberg model we performed classical MC simulation to estimate the Neel temperature ($T_N$) of the $Nb_3I_8$ bilayer [56]. In our MC simulation, a $100 \times 100$ square supercell containing $5 \times 10^4$ local magnetic moments was adopted and the simulated temperature ranges from 0 to 40 K with a step of 5 K. The $T_N$ can be estimated from the temperature dependent specific heat curves, corresponding to the abrupt change in the specific heat [83,84]. The calculated $T_N$ for the $Nb_3I_8$ bilayer is about 10 K, which is comparable with the $VOF_2$ ($\sim 15$ K) [85], $VOI_2$ ($\sim 21$ K) [86] and $Cr_2Ge_2Te_6$ ($\sim 30$ K) [87]. In addition, we also use the MC simulation to study the FM transition temperature of $Nb_3I_8$ monolayer, and the simulated Curie temperatures are about 25 K.

For the $AFE_{tt}$ bilayer, there are two degenerate AFM configurations, namely $P \uparrow M \uparrow$ and $P \uparrow M \downarrow$, where $P \uparrow$ and $M \downarrow$ denotes, respectively, the polarization directions and magnetism directions of the two layers. Figure 3(c) shows the layer-resolved band structures of $P \uparrow M \downarrow$ configuration. Due to the interlayer AFM coupling, the energy band is spin degenerate with the valley character near the Fermi level. Due to the opposite electric polarization and magnetism direction between the upper layer and lower layer, the Berry curvatures are also opposite for the upper and lower layer. So, under hole doping the layer-resolved spin Hall effect appears since the spin-up (upper layer) and spin-down (lower layer) holes acquire opposite transverse velocities and accumulate towards opposite sides of the sample, as shown in Fig. 3(d). Similar results can be obtained for the $P \downarrow M \uparrow$ configuration [56].

When a vertical external electric field is applied, the spin degeneracy can be lifted due to the interlayer potential difference. The opposite electric field lead to opposite spin splitting
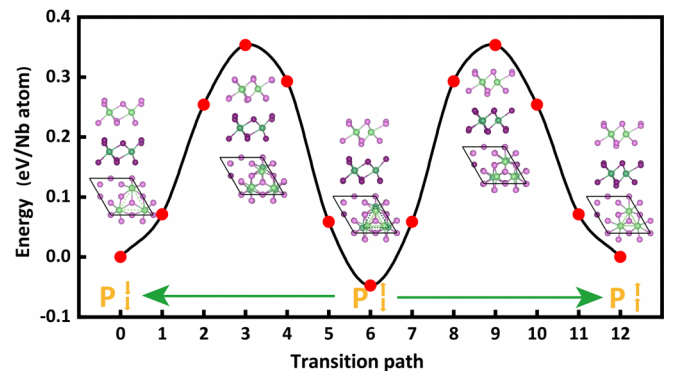


FIG. 4. The transition path of bilayer $Nb_3I_8$ from one FE state to the other opposite FE state.
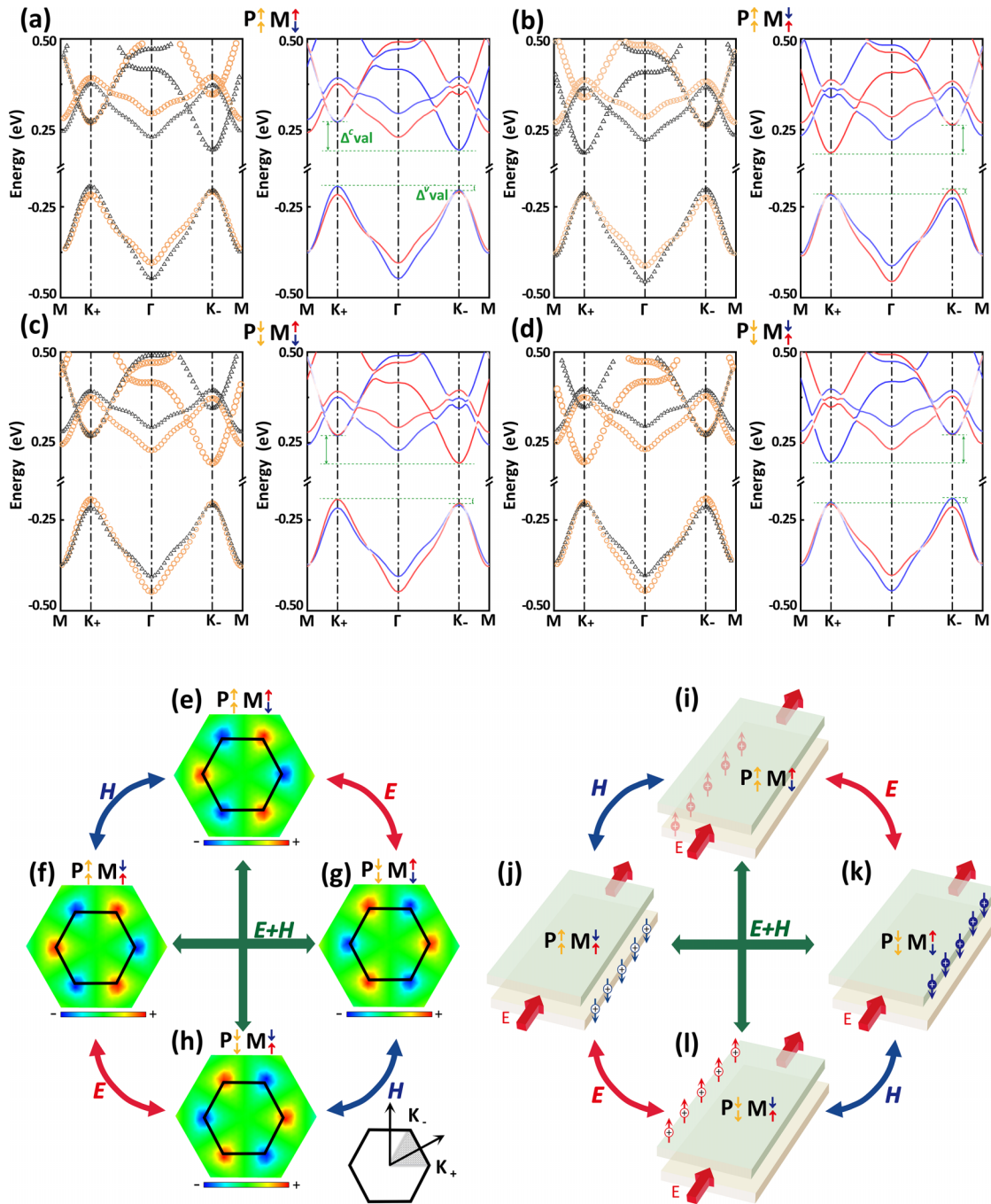
FIG. 5. (a)–(d) Energy bands of bilayer FE configurations with the SOC. Four configurations are classified according to different combinations of the electric polarization and magnetization directions, namely (a)$P\uparrow M\updownarrow$, (b)$P\uparrow M\updownarrow$, (c) $P\downarrow M\updownarrow$, (d) $P\downarrow M\updownarrow$. Layer-resolved bands and spin-resolved bands are shown respectively, where the orange circles and gray triangles represent respectively the contribution of the upper and lower layer, and the red and blue curves represent respectively the spin-up and spin-down channel. (e)–(h) Berry curvature calculated in the momentum space for (e) $P\uparrow M\updownarrow$, (f) $P\uparrow M\updownarrow$, (g) $P\downarrow M\updownarrow$, (h) $P\downarrow M\updownarrow$ configurations. (i)–(l) Schematic diagrams of the anomalous Hall effect for (i) $P\uparrow M\updownarrow$, (j) $P\uparrow M\updownarrow$, (k) $P\downarrow M\updownarrow$, (l) $P\downarrow M\updownarrow$ configurations.

due to the interlayer AFM coupling, as shown in Fig. 3(e). Under hole doping, the anomalous Hall effect can be realized by applying an external electric field, similar to the electric field control of bilayer VSe$_2$ [8]. The direction of the spin and Hall voltage can be reversed by controlling the direction of the electric field, which cannot be realized in monolayer. In addition, for the AFE$_{hh}$ bilayer the similar results can be obtained [56].

### D. The spin/valley/layer-polarized anomalous Hall effect in FE bilayer Nb$_3$I$_8$

When the applied external vertical electric field is further increased, the phase transition from the AFE state to FE state may occur for the bilayer Nb$_3$I$_8$. The transition path obtained by the CINEB method is shown in Fig. 4. Actually, we performed two different FE transition calculations. One is the

calculation from an AFE ($P_\downarrow^\uparrow$) to a FE ($P_\uparrow^\uparrow$) state, and the other is from one FE ($P_\uparrow^\uparrow$) state to the other opposite FE ($P_\downarrow^\downarrow$) state. The results indicate that the transition path from one FE state to the other opposite FE state will pass through the AFE ($P_\downarrow^\uparrow$) state, as shown in Fig. 4. In addition, if the bilayer Nb$_3$I$_8$ is initially in an AFE state, the phase transition from an AFE state to a FE state may occur when a sufficiently large external vertical electric field is applied. During the FE transition the polarization direction of only one layer is reversed, so the transition from an AFE to a FE state actually corresponds to the FE transition of a single layer. The transition energy barrier is 0.4 eV/Nb, which is lower than that of Sc$_2$CO$_2$ (0.52 eV) [88] and comparable with VOF$_2$ (0.33 eV) [85] and most extensively studied multiferroic BiFeO$_3$ (0.427 eV) [89]. In the experiment, BiFeO$_3$ has achieved 180 °FE reversal under the external electric field [90]. Therefore, the polarization reversal is expected to occur experimentally under the external electric field. The large energy barrier indicates the strong stability of the FE state at room temperature, although the total energy of the AFE state is lower by 48 meV/Nb than that of the FE state. Hence, when a positive electric field is introduced, the AFE$_{tt}$ phase $P_\downarrow^\uparrow M_\downarrow^\uparrow$ ($P_\downarrow^\uparrow M_\uparrow^\downarrow$) changes to the FE phase $P_\downarrow^\downarrow M_\downarrow^\uparrow$ ($P_\downarrow^\downarrow M_\uparrow^\downarrow$). When a negative electric field is applied, the $P_\downarrow^\uparrow M_\uparrow^\uparrow$ ($P_\downarrow^\uparrow M_\uparrow^\downarrow$) changes to the opposite FE phase $P_\uparrow^\uparrow M_\downarrow^\uparrow$ ($P_\uparrow^\uparrow M_\uparrow^\downarrow$).

By combining the directions of the electric polarization and magnetization, we obtain four different FE and AFM configurations, $P_\uparrow^\uparrow M_\downarrow^\uparrow$, $P_\uparrow^\uparrow M_\uparrow^\downarrow$, $P_\downarrow^\downarrow M_\downarrow^\uparrow$ and $P_\downarrow^\downarrow M_\uparrow^\downarrow$, with degenerate energy. In addition, we also check the AFM coupling between two layers and found that the interlayer magnetic exchange energy $E_{ex}$ is 8.2 meV/unit cell, indicating the A-type AFM is the ground state. The electric polarization is $0.135 \times 10^{-12}$C/m, which is comparable to the polarization values of InSe ($0.24 \times 10^{-12}$C/m) and GaSe ($0.46 \times 10^{-12}$C/m) [91]. Band structures with the SOC are shown in Figs. 5(a)–5(d). The valley splitting of the valence band and conduction band is 11 and 77 meV, respectively. Different from the AFE bilayer, the energy bands from the upper and lower layers are no longer degenerate due to the potential difference induced by the electric polarization between two layers. In addition, the spin degeneracy is also lifted due to the AFM coupling between two layer. So, only by reversing the polarization direction, we can control spin and layer degree of freedom.

Correspondingly we calculate the Berry curvatures of four different FE configurations $P_\uparrow^\uparrow M_\downarrow^\uparrow$, $P_\uparrow^\uparrow M_\uparrow^\downarrow$, $P_\downarrow^\downarrow M_\downarrow^\uparrow$, $P_\downarrow^\downarrow M_\uparrow^\downarrow$, as shown in Figs. 5(e)–5(h). One of the most important findings is that the sign of the Berry curvature in the $K_+$ and $K_-$ valleys changes when the polarization direction is reversed in Figs. 5(e) and 5(g), while the sign of the valley splitting does not change in Figs. 5(a) and 5(c). Therefore, this indicates that the anomalous Hall effect can be controlled by the external electric field. Under the in-plane electric field, the holes in the $K_+$ and $K_-$ valleys will obtain opposite anomalous velocities and move to the opposite edge of the sample due to the

opposite signs of Berry curvature, as shown in Figs. 5(i)–5(l). For the $P_\uparrow^\uparrow M_\downarrow^\uparrow$, the spin-up holes from the $K_+$ valley of the lower monolayer acquire anomalous velocities proportional to the negative Berry curvatures and then gather at the one side of the sample, achieving the spin/valley/layer-polarized anomalous Hall effect in Fig. 5(i). When the polarization direction is reversed ($P_\downarrow^\downarrow M_\uparrow^\uparrow$), the signs of Berry curvatures of the $K_+$ and $K_-$ valleys are reversed accordingly. In this case, the spin-down holes from $K_+$ valley of the upper monolayer acquire anomalous velocities in the opposite direction and thus concentrate at the opposite edge of the sample, resulting in the measurable opposite Hall voltage in Fig. 5(k). That is, by controlling the electric polarization, we can realize the electric field control of the spin/valley/layer-polarized anomalous Hall effect, providing a possible ways for tuning multiple degree of freedom by pure electric field. In addition, if the direction of the AFM coupling can be controlled, $P_\uparrow^\uparrow M_\downarrow^\uparrow$ can be changed in to $P_\uparrow^\uparrow M_\uparrow^\downarrow$ and thus the spin/valley-polarized anomalous Hall effect can be achieved in Fig. 5(j). Therefore, the multiferroic Nb$_3$I$_8$ bilayer provides a very excellent platform to achieve the effective electric field control of the spin/valley/layer-polarized anomalous Hall effect and provides an alternative scheme for designing nonvolatile electronic information devices by using spin, valley, and layer degrees of freedom.

## IV. CONCLUSIONS

In summary, we study the coupling between the ferroelectricity, ferromagnetism and ferrovalley in a 2D multiferroic Nb$_3$I$_8$ bilayer with the breathing Kagome lattice. We find that the local sublattice symmetry can be controlled by the FE polarization in monolayer Nb$_3$I$_8$. This results in a sublattice-dependent Berry curvature change in momentum space, where the sign reversal of the Berry curvature can be controlled by the FE transition. A LEH model in a 2D honeycomb lattice with two sublattices can well reveal the underlying physical mechanism. Especially, we find that in the Nb$_3$I$_8$ bilayer with A-type AFM coupling, the spin-valley-layer polarized anomalous Hall effect can be controlled by the FE transition, realizing the nonvolatile electric field control of the anomalous Hall effect. This fascinating phenomenon is attributed to the combination of the intrinsic electric polarization, interlayer magnetic coupling, and SOC effect. Therefore, the Nb$_3$I$_8$ bilayer provides an ideal platform for designing nonvolatile memory and switch based on the electric-field control of the spin/valley/layer-dependent Berry curvature.

[1] G. Qin, H. Wang, L. Zhang, Z. Qin, and M. Hu, Giant effect of spin-lattice coupling on the thermal transport in two-dimensional ferromagnetic CrI$_3$, J. Mater. Chem. C **8**, 3520 (2020).

[2] S. Picozzi, Ferroelectric Rashba semiconductors as a novel class of multifunctional materials, Front. Phys. **2**, 10 (2014).

[3] A. Ming and D. Shuai, Charge-mediated magnetoelectricity: From ferroelectric field effect to charge-ordering ferroelectrics, Acta Phys. Sin. **69**, 217502 (2020).

[4] J. Chen, K. Wu, W. Hu, and J. Yang, Spin-orbit coupling in 2d semiconductors: A theoretical perspective, J. Phys. Chem. Lett. **12**, 12256 (2021).

[5] D. Xiao, W. Yao, and Q. Niu, Valley-Contrasting Physics in Graphene: Magnetic Moment and Topological Transport, Phys. Rev. Lett. **99**, 236809 (2007).

[6] W. Tong, S. Gong, X. Wan, and C. Duan, Concepts of ferrovalley material and anomalous valley Hall effect, Nat. Commun. **7**, 13612 (2016).

[7] T. Zhang, X. Xu, B. Huang, Y. Dai, and Y. Ma, 2D spontaneous valley polarization from inversion symmetric single-layer lattices, npj Comput. Mater. **8**, 64 (2022).

[8] W. Tong and C. Duan, Electrical control of the anomalous valley Hall effect in antiferrovalley bilayers, npj Quantum Mater. **2**, 47 (2017).

[9] X. Liu, A. P. Pyatakov, and W. Ren, Magnetoelectric Coupling in Multiferroic Bilayer VS$_2$, Phys. Rev. Lett. **125**, 247601 (2020).

[10] Z. Yu, S. Guan, X. Sheng, W. Gao, and S. A. Yang, Valley-Layer Coupling: A New Design Principle for Valleytronics, Phys. Rev. Lett. **124**, 037701 (2020).

[11] D. Xiao, G. Liu, W. Feng, X. Xu, and W. Yao, Coupled Spin and Valley Physics in Monolayers of MoS$_2$ and Other Group-VI Dichalcogenides, Phys. Rev. Lett. **108**, 196802 (2012).

[12] X. Xu, W. Yao, D. Xiao, and T. F. Heinz, Spin and pseudospins in layered transition metal dichalcogenides, Nat. Phys. **10**, 343 (2014).

[13] H. Zeng, J. Dai, W. Yao, D. Xiao, and X. Cui, Valley polarization in MoS$_2$ monolayers by optical pumping, Nat. Nanotechnol. **7**, 490 (2012).

[14] K. F. Mak, K. He, J. Shan, and T. F. Heinz, Control of valley polarization in monolayer MoS$_2$ by optical helicity, Nat. Nanotechnol. **7**, 494 (2012).

[15] T. Cao, G. Wang, W. Han, H. Ye, C. Zhu, J. Shi, Q. Niu, P. Tan, E. Wang, B. Liu, and J. Feng, Valley-selective circular dichroism of monolayer molybdenum disulphide, Nat. Commun. **3**, 887 (2012).

[16] G. Aivazian, Z. Gong, A. M. Jones, R. Chu, J. Yan, D. G. Mandrus, C. Zhang, D. Cobden, W. Yao, and X. Xu, Magnetic control of valley pseudospin in monolayer WSe2, Nat. Phys. **11**, 148 (2015).

[17] X. Zhang, T. Cao, Z. Lu, Y. Lin, F. Zhang, Y. Wang, Z. Li, J. C. Hone, J. A. Robinson, D. Smirnov, S. G. Louie, and T. F. Heinz, Magnetic brightening and control of dark excitons in monolayer WSe2, Nat. Nanotechnol. **12**, 883 (2017).

[18] D. MacNeill, C. Heikes, K. F. Mak, Z. Anderson, A. Kormányos, V. Zólyomi, J. Park, and D. C. Ralph, Breaking of Valley Degeneracy by Magnetic Field in Monolayer MoSe$_2$, Phys. Rev. Lett. **114**, 037401 (2015).

[19] Y. Li, J. Ludwig, T. Low, A. Chernikov, X. Cui, G. Arefe, Y. D. Kim, A. M. van der Zande, A. Rigosi, H. M. Hill, S. H. Kim, J. Hone, Z. Li, D. Smirnov, and T. F. Heinz, Valley Splitting and Polarization by the Zeeman Effect in Monolayer MoSe$_2$, Phys. Rev. Lett. **113**, 266804 (2014).

[20] A. Srivastava, M. Sidler, A. V. Allain, D. S. Lembke, A. Kis, and A. Imamoglu, Valley Zeeman effect in elementary optical excitations of monolayer WSe$_2$, Nat. Phys. **11**, 141 (2015).

[21] F. Zhang, J. Jung, G. A. Fiete, Q. Niu, and A. H. MacDonald, Spontaneous Quantum Hall States in Chirally Stacked Few-Layer Graphene Systems, Phys. Rev. Lett. **106**, 156801 (2011).

[22] E. J. Sie, J. McIver, Y. Lee, L. Fu, J. Kong, and N. Gedik, Valley-selective optical Stark effect in monolayer WS$_2$, Nat. Mater. **14**, 290 (2015).

[23] R. Peng, Y. Ma, S. Zhang, B. Huang, and Y. Dai, Valley polarization in janus single-layer mosse via magnetic doping, J. Phys. Chem. Lett. **9**, 3612 (2018).

[24] X. Xu, Y. Ma, T. Zhang, C. Lei, B. Huang, and Y. Dai, Nonmetal-atom-doping-induced valley polarization in single-layer Tl2O, J. Phys. Chem. Lett. **10**, 4535 (2019).

[25] A. N. Andriotis and M. Menon, Tunable magnetic properties of transition metal doped MoS$_2$, Phys. Rev. B **90**, 125304 (2014).

[26] Y. Cheng, Q. Zhang, and U. Schwingenschlögl, Valley polarization in magnetically doped single-layer transition-metal dichalcogenides, Phys. Rev. B **89**, 155429 (2014).

[27] R. Mishra, W. Zhou, S. J. Pennycook, S. T. Pantelides, and J.-C. Idrobo, Long-range ferromagnetic ordering in manganese-doped two-dimensional dichalcogenides, Phys. Rev. B **88**, 144409 (2013).

[28] A. Ramasubramaniam and D. Naveh, Mn-doped monolayer MoS$_2$: An atomically thin dilute magnetic semiconductor, Phys. Rev. B **87**, 195201 (2013).

[29] Y. Cheng, Z. Zhu, W. Mi, Z. Guo, and U. Schwingenschloegl, Prediction of two-dimensional diluted magnetic semiconductors: Doped monolayer MoS$_2$ systems, Phys. Rev. B **87**, 100401 (2013).

[30] J. Qi, X. Li, Q. Niu, and J. Feng, Giant and tunable valley degeneracy splitting in MoTe$_2$, Phys. Rev. B **92**, 121403 (2015).

[31] Q. Zhang, S. A. Yang, W. Mi, Y. Cheng, and U. Schwingenschlogl, Large Spin-Valley Polarization in Monolayer MoTe$_2$ on Top of EuO(111), Adv. Mater. **28**, 959 (2016).

[32] A. Zhang, K. Yang, Y. Zhang, A. Pan, and M. Chen, Electrically switchable valley polarization, spin/valley filter, and valve effects in transition-metal dichalcogenide monolayers interfaced with two-dimensional ferromagnetic semiconductors, Phys. Rev. B **104**, L201403 (2021).

[33] C. Ke, Y. Wu, W. Yang, Z. Wu, C. Zhang, X. Li, and J. Kang, Large and controllable spin-valley splitting in two-dimensional WS2/h-VN heterostructure, Phys. Rev. B **100**, 195435 (2019).

[34] B. Zhou, Z. Li, J. Wang, X. Niu, and C. Luan, Tunable valley splitting and an anomalous valley Hall effect in hole-doped WS2 by proximity coupling with a ferromagnetic MnO$_2$ monolayer, Nanoscale **11**, 13567 (2019).

[35] H. Wang and X. Qian, Two-dimensional multiferroics in monolayer group IV monochalcogenides, 2D Mater. **4**, 015042 (2017).

[36] J. Zhang, X. Shen, Y. Wang, C. Ji, Y. Zhou, J. Wang, F. Huang, and X. Lu, Design of Two-Dimensional Multiferroics with Direct Polarization-Magnetization Coupling, Phys. Rev. Lett. **125**, 017601 (2020).

[37] S. Dong, J. M. Liu, S. W. Cheong, and Z. F. Ren, Multiferroic materials and magnetoelectric physics: Symmetry, entanglement, excitation, and topology, Adv. Phys. **64**, 519 (2015).

[38] R. Ramesh and N. A. Spaldin, Multiferroics: Progress and prospects in thin films, Nat. Mater. **6**, 21 (2007).

[39] N. A. Spaldin and R. Ramesh, Advances in magnetoelectric multiferroics, Nat. Mater. **18**, 203 (2019).

[40] J. Zhang, L. Lin, Y. Zhang, M. Wu, B. I. Yakobson, and S. Dong, Type-II multiferroic Hf2VC2F2 mxene monolayer with high transition temperature, J. Am. Chem. Soc. **140**, 9768 (2018).

[41] W. Luo, K. Xu, and H. Xiang, Two-dimensional hyperferroelectric metals: A different route to ferromagnetic-ferroelectric multiferroics, Phys. Rev. B **96**, 235415 (2017).

[42] J. Qi, H. Wang, X. Chen, and X. Qian, Two-dimensional multiferroic semiconductors with coexisting ferroelectricity and ferromagnetism, Appl. Phys. Lett. **113**, 043102 (2018).

[43] Y. Lai, Z. Song, Y. Wan, M. Xue, C. Wang, Y. Ye, L. Dai, Z. Zhang, W. Yang, H. Du, and J. Yang, Two-dimensional ferromagnetism and driven ferroelectricity in van der Waals CuCrP2S6, Nanoscale **11**, 5163 (2019).

[44] C. Gong, E. M. Kim, Y. Wang, G. Lee, and X. Zhang, Multiferroicity in atomic van der Waals heterostructures, Nat. Commun. **10**, 2657 (2019).

[45] W. Kohn and L. J. Sham, Self-consistent equations including exchange and correlation effects, Phys. Rev. **140**, A1133 (1965).

[46] G. Kresse and J. Furthmüller, Efficient iterative schemes for *ab initio* total-energy calculations using a plane-wave basis set, Phys. Rev. B **54**, 11169 (1996).

[47] P. E. Blöchl, Projector augmented-wave method, Phys. Rev. B **50**, 17953 (1994).

[48] J. P. Perdew, K. Burke, and M. Ernzerhof, Generalized Gradient Approximation Made Simple, Phys. Rev. Lett. **77**, 3865 (1996).

[49] T. Bučko, J. Hafner, S. Lebègue, and J. G. Ángyán, Improved description of the structure of molecular and layered crystals: Ab initio dft calculations with van der waals corrections, J. Phys. Chem. A **114**, 11814 (2010).

[50] S. Grimme, Semiempirical GGA-type density functional constructed with a long-range dispersion correction, J. Comput. Chem. **27**, 1787 (2006).

[51] H. J. Monkhorst and J. D. Pack, Special points for Brillouin-zone integrations, Phys. Rev. B **13**, 5188 (1976).

[52] V. I. Anisimov, J. Zaanen, and O. K. Andersen, Band theory and Mott insulators: Hubbard U instead of Stoner I, Phys. Rev. B **44**, 943 (1991).

[53] V. I. Anisimov, I. V. Solovyev, M. A. Korotin, M. T. Czyżyk, and G. A. Sawatzky, Density-functional theory and NiO photoemission spectra, Phys. Rev. B **48**, 16929 (1993).

[54] V. I. Anisimov, F. Aryasetiawan, and A. I. Lichtenstein, First-principles calculations of the electronic structure and spectra of strongly correlated systems: The LDA+U method, J. Phys.: Condens. Matter **9**, 767 (1997).

[55] J. Jiang, Q. Liang, R. Meng, Q. Yang, C. Tan, X. Sun, and X. Chen, Exploration of new ferromagnetic, semiconducting and biocompatible Nb3X8 (X = Cl, Br or I) monolayers with considerable visible and infrared light absorption, Nanoscale **9**, 2992 (2017).

[56] See Supplemental Material at http://link.aps.org/supplemental/10.1103/PhysRevB.108.115407 for more information about the results for different Ueff values, the classic Monte Carlo simulation, the band structures without the SOC, the different magnetic configurations, the results for the AFEtt configuration and the results for the AFEhh bilayer,

[57] G. Henkelman, B. P. Uberuaga, and H. Jonsson, A climbing image nudged elastic band method for finding saddle points and minimum energy paths, J. Chem. Phys. **113**, 9901 (2000).

[58] S. Smidstrup, A. Pedersen, K. Stokbro, and H. Jonsson, Improved initial guess for minimum energy path calculations, J. Chem. Phys. **140**, 214106 (2014).

[59] T. Fukui, Y. Hatsugai, and H. Suzuki, Chern numbers in discretized Brillouin zone: Efficient method of computing (spin) Hall conductances, J. Phys. Soc. Jpn. **74**, 1674 (2005).

[60] S. N. Magonov, P. Zonnchen, H. Rotter, H. J. Cantow, G. Thiele, J. Ren, and M. H. Whangbo, Scanning tunneling and atomic force microscopy study of layered transition metal halides Nb3X8 (X = C1, Br, I), J. Am. Chem. Soc. **115**, 2495 (1993).

[61] S. Oh, K. H. Choi, S. Chae, B. J. Kim, B. J. Jeong, S. H. Lee, J. Jeon, Y. Kim, S. S. Nanda, L. Shi, D. K. Yi, J.-H. Lee, H. K. Yu, and J.-Y. Choi, Large-area synthesis of van der Waals two-dimensional material Nb3I8 and its infrared detection applications, J. Alloys Compd. **831**, 154877 (2020).

[62] B. J. Kim, B. J. Jeong, S. Oh, S. Chae, K. H. Choi, S. S. Nanda, T. Nasir, S. H. Lee, K.-W. Kim, H. K. Lim, L. Chi, I. J. Choi, M.-K. Hong, D. K. Yi, H. K. Yu, J.-H. Lee, and J.-Y. Choi, Structural and electrical properties of Nb3I8 layered crystal, Phys. Status Solid.-Rapid Res. Lett. **13**, 1800448 (2019).

[63] F. Conte, D. Ninno, and G. Cantele, Layer-dependent electronic and magnetic properties of Nb3I8, Phys. Rev. Res. **2**, 033001 (2020).

[64] Y. Li, C. Liu, G.-D. Zhao, T. Hu, and W. Ren, Two-dimensional multiferroics in a breathing Kagome lattice, Phys. Rev. B **104**, L060405 (2021).

[65] G. Cantele, F. Conte, L. Zullo, and D. Ninno, Tunable electronic and magnetic properties of thin Nb3I8 nanofilms: Interplay between strain and thickness, Phys. Rev. B **106**, 085418 (2022).

[66] R. Peng, Y. Ma, X. Xu, Z. He, B. Huang, and Y. Dai, Intrinsic anomalous valley Hall effect in single-layer Nb3I8, Phys. Rev. B **102**, 035412 (2020).

[67] F. Liu, L. You, K. L. Seyler, X. Li, P. Yu, J. Lin, X. Wang, J. Zhou, H. Wang, H. He, S. T. Pantelides, W. Zhou, P. Sharma, X. Xu, P. M. Ajayan, J. Wang, and Z. Liu, Room-temperature ferroelectricity in CuInP2S6 ultrathin flakes, Nat. Commun. **7**, 12357 (2016).

[68] G. Yu, A. Pan, and M. Chen, Interface engineering of ferroelectricity in thin films of thiophosphate ABP2X6 (A = Cu, Ag; B = In, Bi, Cr, V; X = S, Se), Phys. Rev. B **104**, 224102 (2021).

[69] Y. Zhou, D. Wu, Y. Zhu, Y. Cho, Q. He, X. Yang, K. Herrera, Z. Chu, Y. Han, M. C. Downer, H. Peng, and K. Lai, Out-of-plane piezoelectricity and ferroelectricity in layered $\alpha$-In2Se3 nanoflakes, Nano Lett. **17**, 5508 (2017).

[70] W. Wan, C. Liu, W. Xiao, and Y. Yao, Promising ferroelectricity in 2D group IV tellurides: A first-principless study, Appl. Phys. Lett. **111**, 132904 (2017).

[71] R. Fei, W. Kang, and L. Yang, Ferroelectricity and Phase Transitions in Monolayer Group-IV Monochalcogenides, Phys. Rev. Lett. **117**, 097601 (2016).

[72] S. Guan, C. Liu, Y. Lu, Y. Yao, and S. A. Yang, Tunable ferroelectricity and anisotropic electric transport in monolayer beta-GeSe, Phys. Rev. B **97**, 144104 (2018).

[73] J. Kim, K. W. Kim, D. Shin, S. H. Lee, J. Sinova, N. Park, and H. Jin, Prediction of ferroelectricity-driven Berry curvature enabling charge- and spin-controllable photocurrent in tin telluride monolayers, Nat. Commun. **10**, 3965 (2019).

[74] W. Luo, J. Ji, P. Chen, Y. Xu, L. Zhang, H. Xiang, and L. Bellaiche, Nonlinear phonon Hall effects in ferroelectrics: Existence and nonvolatile electrical control, Phys. Rev. B **107**, L241107 (2023).

[75] H. Wang and X. Qian, Ferroelectric nonlinear anomalous Hall effect in few-layer WTe2, npj Comput. Mater. **5**, 119 (2019).

[76] Z. Song, X. Sun, J. Zheng, F. Pan, Y. Hou, M.-H. Yung, J. Yang, and J. Lu, Spontaneous valley splitting and valley pseudospin field effect transistors of monolayer VAgP2Se6, Nanoscale **10**, 13986 (2018).

[77] P. Zhao, Y. Ma, C. Lei, H. Wang, B. Huang, and Y. Dai, Single-layer LaBr2: Two-dimensional valleytronic semiconductor with spontaneous spin and valley polarizations, Appl. Phys. Lett. **115**, 261605 (2019).

[78] X. Li, T. Cao, Q. Niu, J. Shi, and J. Feng, Coupling the valley degree of freedom to antiferromagnetic order, Proc. Nat. Acad. Sci. USA **110**, 3738 (2013).

[79] Y. Yao, Y. Liang, D. Xiao, Q. Niu, S.-Q. Shen, X. Dai, and Z. Fang, Theoretical evidence of the Berry-phase mechanism in anomalous Hall transport: First-principles studies of $CuCr_2Se_{4-x}Br_x$, Phys. Rev. B **75**, 020401 (2007).

[80] N. Sivadas, S. Okamoto, X. Xu, C. J. Fennie, and D. Xiao, Stacking-dependent magnetism in bilayer $CrI_3$, Nano Lett. **18**, 7658 (2018).

[81] W. Chen, Z. Sun, Z. Wang, L. Gu, X. Xu, S. Wu, and C. Gao, Direct observation of van der Waals stacking-dependent interlayer magnetism, Science **366**, 983 (2019).

[82] X. Kong, H. Yoon, M. J. Han, and L. Liang, Switching interlayer magnetic order in bilayer CrI3 by stacking reversal, Nanoscale **13**, 16172 (2021).

[83] Y. Sun, Z. Zhuo, X. Wu, and J. Yang, Room-temperature ferromagnetism in two-dimensional Fe2Si nanosheet with enhanced spin-polarization ratio, Nano Lett. **17**, 2771 (2017).

[84] W. Wang, S. Dai, X. Li, J. Yang, D. J. Srolovitz, and Q. Zheng, Measurement of the cleavage energy of graphite, Nat. Commun. **6**, 7853 (2015).

[85] H. You, N. Ding, J. Chen, and S. Dong, Prediction of two-dimensional ferromagnetic ferroelectric VOF2 monolayer, Phys. Chem. Chem. Phys. **22**, 24109 (2020).

[86] N. Ding, J. Chen, S. Dong, and A. Stroppa, Ferroelectricity and ferromagnetism in a VOI2 monolayer: Role of the Dzyaloshinskii-Moriya interaction, Phys. Rev. B **102**, 165129 (2020).

[87] C. Gong, L. Li, Z. Li, H. Ji, A. Stern, Y. Xia, T. Cao, W. Bao, C. Wang, Y. Wang, Z. Q. Qiu, R. J. Cava, S. G. Louie, J. Xia, and X. Zhang, Discovery of intrinsic ferromagnetism in two-dimensional van der Waals crystals, Nature (London) **546**, 265 (2017).

[88] A. Chandrasekaran, A. Mishra, and A. K. Singh, Ferroelectricity, antiferroelectricity, and ultrathin 2d electron/hole gas in multifunctional monolayer MXene, Nano Lett. **17**, 3290 (2017).

[89] P. Ravindran, R. Vidya, A. Kjekshus, H. Fjellvag, and O. Eriksson, Theoretical investigation of magnetoelectric behavior in $BiFeO_3$, Phys. Rev. B **74**, 224412 (2006).

[90] C. Chen, D. Chen, P. Li, M. Qin, X. Lu, G. Zhou, X. Gao, and J. Liu, Deterministic manipulation of multi-state polarization switching in multiferroic thin films, Adv. Funct. Mater. **33**, 2208244 (2023).

[91] L. Li and M. Wu, Binary compound bilayer and multilayer with vertical polarizations: two-dimensional ferroelectrics, multiferroics, and nanogenerators, ACS Nano **11**, 6382 (2017).